AFRL-RZ-WP-TP-2012-0194

SIMULATION OF DISTORTION GENERATION IN A MODERN SERPENTINE DIFFUSER TO IMPROVE EXPERIMENTAL EFFECTIVENESS (PREPRINT)

Darius D. Sanders and Michael G. List

Fan/Compressor Branch
Turbine Engine Division

MAY 2012

AIR FORCE RESEARCH LABORATORY
PROPULSION DIRECTORATE
WRIGHT-PATTERSON AIR FORCE BASE, OH 45433-7251
AIR FORCE MATERIEL COMMAND
UNITED STATES AIR FORCE

REPORT DOCUMENTATION PAGE

Form Approved
OMB No. 0704-0188

1. REPORT DATE *(DD-MM-YY)*	2. REPORT TYPE	3. DATES COVERED *(From - To)*
May 2012	Technical Paper Preprint	01 October 2010 – 02 April 2012

4. TITLE AND SUBTITLE
SIMULATION OF DISTORTION GENERATION IN A MODERN SERPENTINE DIFFUSER TO IMPROVE EXPERIMENTAL EFFECTIVENESS (PREPRINT)

5a. CONTRACT NUMBER
In-house

5b. GRANT NUMBER

5c. PROGRAM ELEMENT NUMBER
62203F

6. AUTHOR(S)
Darius D. Sanders and Michael G. List

5d. PROJECT NUMBER
3066

5e. TASK NUMBER
TK

5f. WORK UNIT NUMBER
306604TK

7. PERFORMING ORGANIZATION NAME(S) AND ADDRESS(ES)
Fan/Compressor Branch (AFRL/RZTF)
Turbine Engine Division
Air Force Research Laboratory, Propulsion Directorate
Wright-Patterson Air Force Base, OH 45433-7251
Air Force Materiel Command, United States Air Force

8. PERFORMING ORGANIZATION REPORT NUMBER
AFRL-RZ-WP-TP-2012-0194

9. SPONSORING/MONITORING AGENCY NAME(S) AND ADDRESS(ES)
Air Force Research Laboratory
Propulsion Directorate
Wright-Patterson Air Force Base, OH 45433-7251
Air Force Materiel Command
United States Air Force

10. SPONSORING/MONITORING AGENCY ACRONYM(S)
AFRL/RZTF

11. SPONSORING/MONITORING AGENCY REPORT NUMBER(S)
AFRL-RZ-WP-TP-2012-0194

12. DISTRIBUTION/AVAILABILITY STATEMENT
Approved for public release; distribution unlimited.

13. SUPPLEMENTARY NOTES
PA Case Number: 88ABW-2012-3032; Clearance Date: 29 May 2012. Technical paper contains color.

14. ABSTRACT
Modern serpentine diffusers create distorted flowfields which are ingested by embedded propulsion systems. Fundamental research into the generation and content of such distortion patterns is necessary to better understand inlet conditions for the engine. Simulation of the diffuser provided a number of insights for a complementary experimental program including particle image velocity (PIV) plane placement and seeding locations, necessary resolution of measurement, and expected operational range and conditions. Analysis of the results provided better definition of some experimental requirements and sensitivities for capturing multiple per-rev distortions. In comparing with preliminary experimental results, it was determined that diffuser flowfield simulations may require detached-eddy simulation (DES) or large-eddy simulation (LES) to properly capture flow feature position and the impact of the separation regions.

15. SUBJECT TERMS
serpentine diffuser, computational fluid dynamics, wind tunnel

16. SECURITY CLASSIFICATION OF:			17. LIMITATION OF ABSTRACT:	18. NUMBER OF PAGES	19a. NAME OF RESPONSIBLE PERSON (Monitor)
a. REPORT	b. ABSTRACT	c. THIS PAGE			Steven L. Puterbaugh
Unclassified	Unclassified	Unclassified	SAR	16	19b. TELEPHONE NUMBER *(Include Area Code)* N/A

Simulation of Distortion Generation in a Modern Serpentine Diffuser to Improve Experimental Effectiveness

Darius D. Sanders and Michael G. List
Fans and Compressors Branch, AFRL/RZTF
Air Force Research Laboratory
WPAFB, OH 45433
{darius.sanders,michael.list}@wpafb.af.mil

May 16, 2012

Abstract

Modern serpentine diffusers create distorted flowfields which are ingested by embedded propulsion systems. Fundamental research into the generation and content of such distortion patterns is necessary to better understand inlet conditions for the engine. Simulation of the diffuser provided a number of insights for a complementary experimental program including PIV plane placement and seeding locations, necessary resolution of measurement, and expected operational range and conditions. Analysis of the results provided better definition of some experimental requirements and sensitivities for capturing multiple per-rev distortions. In comparing with preliminary experimental results, it was determined that diffuser flowfield simulations may require DES or LES to properly capture flow feature position and the impact of the separation regions.

Nomenclature

α	Swirl angle
θ	Circumferential extent
C_θ	Tangential velocity
C_x	Axial velocity
i	Ring index
k	Sub-region within a ring
N	Number of probe rings
Q	Number of sub-regions within a ring

1 Introduction

Embedded engine applications subject turbomachinery to nonuniform total pressure, total temperature, static pressure, and flow angle (swirl). Additional sources of distorted flow include maneuvers, boundary layer formation, separations, and hot gas ingestion. Tangible changes in performance and operability occur when nonuniformities impinge upon the fan or compressor face. Modern aircraft systems deliver high spatial frequency content distortion patterns at the fan face which are not well understood. To adequately quantify the impact of distortion generated by a modern serpentine diffuser upon a high performance transonic fan, a combined experimental and numerical program has been formulated to conduct detailed investigations, extract pertinent physics, and formulate design guidance to mitigate the negative impacts of distortion. The current document specifically addresses CFD and analysis of the isolated diffuser to augment experimental testing of such and ultimately to support preparation for a combined diffuser-fan experiment. Numerical investigations of the diffuser preceded the experimental investigation for predictive purposes. Additional CFD analyses will be conducted to correct discrepancies found as the experimental data is collected.

During the first phase of the program, CFD methods were used to study the flowfield of an inlet diffuser configuration and support experiments conducted in an annular cascade facility (ACF). The ACF is shown in Figure 1(a). The steady pressure distortion field was measured with total pressure rakes positioned at the diffuser discharge, or Aerodynamic Interface Plane (AIP) (see Figure 1(b)), in the isolated test configuration. With this data, screens will be developed to simulate this distortion field in front of the transonic fan. Also during this phase, steady and time-resolved velocity and pressure field measurements at the AIP have been obtained through Particle Image Velocity (PIV) measurements and conventional probe arrays [1]. Specific testing details relevant to this discussion are:

- A bellmouth extends from the diffuser throat into the flow barrel to reduce separation entering the diffuser.
- Surface static pressures were measured along the diffuser centerline and around the throat location.
- An array of 8 rakes, each containing 10 total pressure measurements was located at the diffuser discharge plane.
- The diffuser assembly could rotate in 1° increments, making it possible to create highly resolved time-averaged datasets.

The next phases incorporate learning from the first phase to analyze distortion transfer and impact on a transonic fan and ultimately to determine coupling effects between the diffuser and fan. Through the use of CFD analysis a positive impact has been seen on the planning, evolution, and data processing of the corresponding experimental effort. This study expanded the ability to complete rapid CFD analysis of advanced inlet geometries and provided guidance for future measurement techniques.

2 Methodology

2.1 Computational Fluid Dynamics

Steady and unsteady simulations of the isolated serpentine diffuser geometry as well as the diffuser with the upstream flow conditioning barrel were conducted using the commercial CFD solver StarCCM+ [2]. A number of additional codes were previously used for RANS simulation of the diffuser, but the StarCCM+ solution was determined to be typical of a range of the solvers used. The flow barrel was not simulated with the other solvers.

An unstructured polyhedral mesh topology was generated using StarCCM+'s internal mesh generator. A total cell count of 3.3M cells was used for the isolated diffuser and a total of 6.8M cells was used for the diffuser with a flow barrel. Prism cells were used to resolve viscous effects from the wall with a $y+$ range of 5 to 30 while pure polyhedral cells were used in the flowpath.

Solutions were obtained using the RANS solver with a 2nd order upwind spatial discretization. For unsteady simulations 2nd order temporal discretization was employed with a time step of 10 μs. Flowfield convergence was considered achieved after residuals decreased below 1×10^{-4}. The k-ω SST turbulence model was used.

In the isolated diffuser simulations the inlet boundary condition was an imposition of total pressure, total temperature, and flow angle upstream of the bellmouth. For simulations with the flow barrel a massflow inlet was used in order to obtain a desired throat Mach number. In both simulations a constant static pressure was applied at a plane downstream of the AIP.

Without the flow barrel a steady state solution was obtained and the standing distortion pattern was found. Incorporation of the flow barrel required an unsteady solution due to recirculation regions behind the diffuser's bellmouth but within the barrel. To mitigate the impact of time-variation on the analyses, an average was taken over a series of aperiodic events in a manner similar to a running average used in the facility — in fact, the same temporal duration was averaged numerically and experimentally, 0.06s, a lengthy time-scale relative to the fan.

Qualitative flow analysis was completed on the time-averaged and unsteady flowfields using Fieldview and various flow visualization techniques to investigate the vortical structures produced by the diffuser. The AIP was extracted using Tecplot and its interpolation utilities. The extracted total pressure and swirl angle are the basis for the following analyses.

The full process to simulate one facility flow rate steady state used 48 cores. With the flow barrel included, the unsteady simulations required 80 cores each. Total processor hour usage for the investigation was 50000 CPH on the Raptor (Cray XE6) system at the AFRL DSRC. The total turnaround for each simulation, including post-processing, was 3 weeks.

2.2 Distortion Descriptors

Experimental data is only available at probe locations. In order to simulate the experimental probe locations at the AIP, a mesh was created for comparisons to the experimental measurements. The circumferential location, number of probes per rake, and number of rakes could be set and adjusted. Bilinear interpolation was used to set the value at each probe location. The configuration is denoted as $nprobes \times nrakes$ where $nprobes$ represents the number of probes on a given rake and $nrakes$ is the number of equi-spaced rakes around the annulus. The configuration recommended by the SAE S-16 committee was 5 probes with 8 rakes, 5×8, and is shown in Figure 1(b). The probes are located at the centroids of equal areas of the annulus. The probes located at the same radius are grouped as a ring.

Traditional distortion descriptors for total pressure deficit were reported in AIR 1419 [3]. The average pressure around the annulus at a given radius is seen in Eq. 1 and the area-averaged low pressure regions are computed using Eq. 2. The extent of

a region of low total pressure on a given ring, i, is computed by subtracting the beginning and ending locations and is denoted by θ_{ik}^{-}. The distortion intensity is given in Eq. 3 and the multiple per-rev content is given in Eq. 4.

$$(PAV)_i = \frac{1}{360}\int_0^{360} P(\theta)_i \mathrm{d}\theta \tag{1}$$

$$(PAVLOW)_i = \frac{1}{\theta_i^{-}}\sum_{k=1}^{Q}\int_{\theta_{ik}^{-}} P(\theta)_i \mathrm{d}\theta \tag{2}$$

$$\left(\frac{\Delta PC}{P}\right)_i = \frac{(PAV)_i - (PAVLOW)_i}{(PAV)_i} = \frac{\sum_{k=1}^{Q}\left(\frac{\Delta PC}{P}\right)_{ik}\theta_{ik}^{-}}{\sum_{k=1}^{Q}\theta_{ik}^{-}} \tag{3}$$

$$(MPR)_i = \frac{\sum_{k=1}^{Q}\left[\left(\frac{\Delta PC}{P}\right)_{ik}\theta_{ik}^{-}\right]}{\max_{k=1,Q}\left[\left(\frac{\Delta PC}{P}\right)_{ik}\theta_{ik}^{-}\right]} \tag{4}$$

The radial intensity of the total pressure distortion requires computation of the face averaged total pressure, Eq. 5. The radial intensity is Eq. 6.

$$(PFAV) = \frac{1}{N}\sum_{i=1}^{N}(PAV)_i \tag{5}$$

$$\left(\frac{\Delta PR}{P}\right)_i = \frac{(PFAV) - (PAV)_i}{(PFAV)} \tag{6}$$

The swirl descriptors were computed using the same Python tools as the traditional distortion descriptors. Equations were taken from [4]. Swirl is defined as $\alpha = \tan^{-1}(C_\theta/C_x)$. The sector swirl (Eq. 7) is the average value of the swirl angle in a region where positive or negative swirl exists. The swirl intensity is computed by Eq. 8 and represents the extent-weighted swirl magnitude. The swirl directivity is shown in Eq. 9. The directivity represents the equivalent bulk swirl motion of the flowfield. The swirl pairs indicates the number of swirl pairs which exist in the flowfield and can be computed via Eq. 10.

$$SS_{i,k}^{\pm} = \frac{1}{\theta_{i,k}^{\pm}}\int_{\theta_{i,k}^{\pm}} \alpha(\theta)_{i,k}\mathrm{d}\theta \tag{7}$$

$$SI_i = \frac{\sum_{k=1}^{m} SS_{i,k}^{+}\times\theta_{i,k}^{-} + \sum_{k=1}^{m}\left|SS_{i,k}^{-}\right|\times\theta_{i,k}^{-}}{360} \tag{8}$$

$$SD_i = \frac{\sum_{k=1}^{m} SS_{i,k}^{+}\times\theta_{i,k}^{-} + \sum_{k=1}^{m} SS_{i,k}^{-}\times\theta_{i,k}^{-}}{\sum_{k=1}^{m} SS_{i,k}^{+}\times\theta_{i,k}^{-} + \sum_{k=1}^{m}\left|SS_{i,k}^{-}\right|\times\theta_{i,k}^{-}} \tag{9}$$

$$SP_i = \frac{\sum_{k=1}^{m} SS_{i,k}^{+}\times\theta_{i,k}^{-} + \sum_{k=1}^{m}\left|SS_{i,k}^{-}\right|\times\theta_{i,k}^{-}}{2\times\max_{k=1,m}\left(SS_{i,k}^{+}\times\theta_{i,k}^{+}, \left|SS_{i,k}^{-}\times\theta_{i,k}^{-}\right|\right)} \tag{10}$$

In order to compute the distortion descriptors a piecewise linear function class was developed in Python. This class enabled rapid integration and extraction of the regions above and below the function mean value. The CARL Python Utilities [5] have been augmented with this linear spline capability.

3 Results

Figure 2 shows the diffuser and flow barrel system with streamlines indicating the important flow features. Streamtraces are colored by Mach number while the diffuser discharge is colored by total pressure recovery. Moving from left to right, a number of physical phenomena can be seen.

Within the flow barrel a large recirculation zone was seen behind the bellmouth of the diffuser. This unsteady region made it necessary to utilize unsteady simulations and time average to obtain results.

Next, as the flow enters the bellmouth and reaches the throat a rapid acceleration was seen. The bellmouth performed well in eliminating separations and straightening the flow. The top-to-bottom asymmetry of the diffuser throat generates a vortex at each of the starboard and port sides. These vortices were seen at the diffuser discharge located at the sides.

Aft of the recurve location in the diffuser the streamtraces converge near top dead center (TDC) and form a pair of tightly wound vortices. This roll up was a direct result of the separation region (denoted by the large bundle of blue streamtraces upstream of the vortices) which created adequate pressure loss to draw the surrounding flow towards TDC. This pressure loss also generated most of the swirl seen at the diffuser exit.

Preliminary experimental data has been obtained and the results of the discharge instrumentation rakes has been plotted with the CFD results in Figure 3. The total pressure distortion pattern is composed of 4 main flow features. At TDC the tightly wound vortex created by the upper wall separation. Near the sides, designated as 90° and 270°, the vortices formed by the asymmetric bellmouth were seen. At Bottom Dead Center (BDC), or 180°, a boundary layer thickening occurred.

In comparing the CFD results with the preliminary experimental data shown in Figure 3, several discrepancies were noticed. First, the experimental results are not located close enough to the walls to pick up the large total pressure deficit. Next, more loss was seen in each of the CFD flow features than the experimentally captured features. Third, the side vortices were not as tight and are closer to 0° experimentally, indicating unsteadiness and a smearing of the vortices. Finally, the TDC vortices had lifted off the surface in the experiment while the CFD remained close to the surface. Downstream of the discharge in the CFD these vortices did separate from the surface, but the distance was much greater than what has been observed experimentally.

Figure 4 shows the distribution of static pressure through the diffuser at 0° and 180°. Good agreement has been obtained along most of the lower surface. Along the upper surface a sharp drop in pressure was seen as the flow accelerated around the recurve section and separated. Once the CFD diverged from the experimental data the correct values aft of the separated region were not reattained.

3.1 Analysis

As previously discussed, distortion descriptors made possible the consistent analysis of experimental data collected at a series of measurement points. In order to provide *a* priori values for the distortion descriptors which could be measured in the experiment, a number of rake configurations were applied to the CFD results. Two of the rake configurations are discussed here — a 5×8 and a 10×360. The first is the defacto standard specified by AIR 1419 [3] and represents nominal measurements taken for a system without the capability to rotate. The second represents the maximum resolution of the annular cascade facility, where there were 10 probes per rake and the hardware could be rotated at 1° increments to reconstruct the full pattern.

Figure 5 shows the total pressure field from the CFD solution on the left with the discrete probe locations shown in black. The discrete pattern which is formed by the probe values is shown on the right. The pattern is clearly degraded from the smooth CFD contours, demonstrating the loss of fidelity when using the standard 8 rake system. Figure 6 likewise shows the swirl angle. From these discrete probe locations, each of the 5 concentric circles formed by the probes were extracted and used to compute the distortion descriptors. The values per ring have been collected in Table 1.

Table 2 gives the final values for both probe configurations. These values are the average of the values for the concentric circles (recall that the probes are stationed on centers of equal area). There were considerable discrepancies between the two rake configurations, demonstrating the necessity of accurately capturing the flow features through rotation of the distortion pattern when multiple per-rev frequencies exist. In incorporating more integration points, the tangential intensity doubled and the tangential extent was lessened. The pressure distortion is significant but not as high as many observed cases. The swirl distortion parameters indicate that the swirl pattern is close to a 1 per-rev distortion which makes it easier to analyze and can be simulated with the harmonic balance technique. (Note it is clear from Eqs. 5 and 6 that the sum of the radial intensity over the probe rings should be zero.)

The discrepancies in the distortion parameters can be better understood with the average total pressure and swirl angles from the probes, as shown in Figure 7. These averages clearly show the improved spatial resolution and it is clear that integral methods would underpredict values when the full pattern was not taken into account.

Figure 8 shows the circumferential and radial intensities plotted versus radius. The tangential intensity is greatly increased at higher radius when more tangential measurement points are included. This was expected because although the tangential extents of the deficit regions decreased, the deficit region integrated increased sufficiently. The radial intensity is rather well captured by the coarser probe array as the face average value of total pressure in the full CFD solution was relatively close to the value obtained by averaging the probe values.

Figure 9 shows the extent and per-rev components. The circumferential extent, plotted on the left, was computed as the maximum tangential section of distorted flow. Resultantly, increasing the resolution decreases extent as the shape of the flow features was brought into focus. The primary flow features should point the distortion descriptors towards a strong 4 per-rev component which was previously shown by List [2, 6]. In both probe configurations half of the probes were stationed in the

deficit regions and half were in the higher pressure regions. This resulted in an aliasing of the multiple per-rev content as the descriptor was calculated, thus indicating closer to a 2 per-rev distortion.

3.2 Impact on Experimental Effort

The computational effort has positively impacted the experimental work in several key ways. These are described below.

The performance of the bellmouth was investigated, ensuring that any separations and boundary layers were thin. After indicating that the losses in the designed bellmouth were acceptable an estimated loss factor was provided for use in several diffuser calibration measurements.

The choking condition for the diffuser system was discovered experimentally at a lower throat Mach number than expected. A CFD investigation was conducted using a coarse mesh to rapidly map a range of throat Mach numbers and identify the choking Mach number.

Initial CFD studies were used to determine the necessary size and extent of PIV planes. These data were subsequently employed to size and position optical access windows. The initial studies were also used to determine the rotational resolution necessary for the diffuser. Early identification of these needs drastically improved the initial design phases for hardware and eliminated the need for extensive redesigns after fabrication.

The process of seeding any experiment properly for PIV is difficult, especially when velocity data is sought in separated regions. Such a difficulty was compounded by the physics of the diffuser when trying to seed the TDC vortex. In order to determine the proper placement of the seeding array, it was necessary to perform computations including the upstream flow conditioning barrel. Once this solution was obtained, streamtraces integrated both forward and backward from the regions of interest were utilized to designate seeding locations. It was determined that the locations appropriate for seeding the TDC region of the diffuser exit were small and not intuitive.

The time required to collect time-averaged experimental data at a given point made collection of a full 360° distortion pattern infeasible. To determine if a reduced dataset provided an adequate description of the distorted flowfield, the CFD solution was sampled at various intervals for a sensitivity analysis. The number of tangential positions at which data were to be taken and the initial clocking were varied to compute derivatives of the various distortion parameters. Using this method it was possible to determine that rotation intervals between 3° and 5° were appropriate for resolving the dominant flow features. This resulted in time savings and has dramatically increased the number of conditions quantified experimentally.

4 Conclusions

Computational analysis was used to augment experimental investigations of a modern serpentine diffuser and to better understand distorted flowfields which are ingested by embedded propulsion systems. Such information was beneficial to the experimental program not only in the design and fabrication effort but also in elucidating data collection techniques and requirements.

Cast in terms of the distortion descriptors, the diffuser design creates reasonably well behaved flow relative to the most aggressive designs. This makes the diffuser excellent for the scientific goals of the overall program. All of the expected physics were observed within the diffuser but the total pressure deficit will not be enough to aerodynamically disable the fan to which it will be coupled. This is crucial as a comprehensive investigation of the coupling effects of the combined diffuser-fan system begins.

Although the total pressure deficit was not overly aggressive, the operating environment for a transonic fan in close coupling with a serpentine diffuser is hardly ideal. Implications of the distortion for the fan includes reduced pressure ratio and efficiency due to the nonuniform pressure, varying incidence and additional loss generation due to swirl distortion, and early onset of stall due to additional blockage formation and off-design operation of multiple rotor passages.

The diffuser flowfield simulations using the RANS CFD method showed a difference in the prediction of the separation region compared to the preliminary experimental measurements. This suggests that the LES or DES CFD method could provide better prediction of the position and impact on separation regions on AIP distortion.

Acknowledgments

The authors would like to thank the staff of the AFRL/DSRC for tirelessly working to support, train, and provide resources to the HPCMP users. The authors would also like to thank the HPCMP for its support through generous allocations, an incredible CD-adapco support team, and the CARL experimental team — the members of which work incredible feats in the name of science and technology.

References

[1] Copenhaver, W. W., Puterbaugh, S. L., Sanders, D., Nessler, C., and List, M. G., 2011. "Overview of serpentine inlet and transonic fan interaction research program". In 7th Annual Dayton Engineering Sciences Symposium. Presentation and Abstract.

[2] List, M. G., 2011. "Distortion Pattern Analysis for Diffuser-Fan Interaction". In DOD HPCMP Users' Group Conference.

[3] Society of Automotive Engineers, 2007. Inlet Total-Pressure-Distortion Considerations for Gas-Turbine Engines. Aerospace Information Report AIR1419, Rev. B.

[4] Society of Automotive Engineers, 2010. A Methodology for Assessing Inlet Swirl Distortion. Aerospace Information Report AIR5686.

[5] List, M. G., and Car, D., 2009. "Tool and process improvement for high-fidelity compressor simulations". In DoD HPCMP Users Group Conference, IEEE Computer Society, pp. 119–126.

[6] List, M. G., 2011. "Impact of spatial multi-frequency distortion patterns on fan performance". In 7th Annual Dayton Engineering Sciences Symposium. Presentation and Abstract.

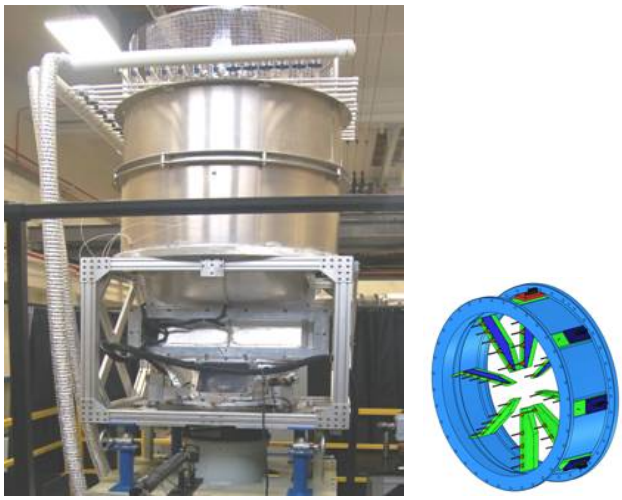

(a) Annular Cascade Facility (b) Rake Case

Figure 1: Annular Cascade Facility with diffuser and flow barrel and the rake case.

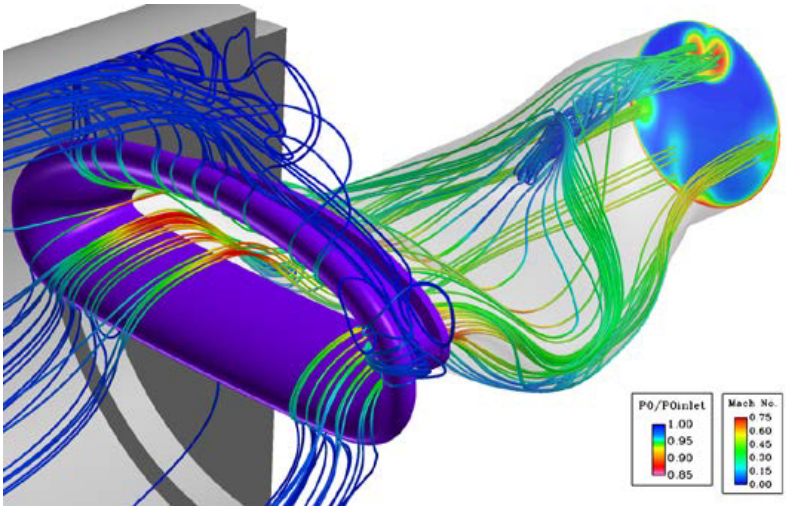

Figure 2: Diffuser flowfield, including upstream flow barrel, shown with streamtraces.

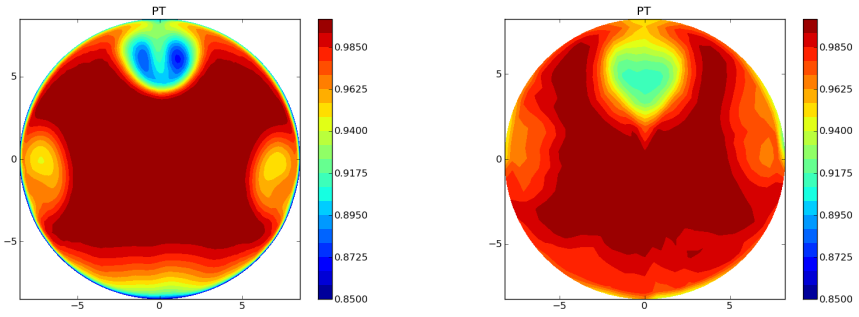

(a) Computational (b) Preliminary Experimental

Figure 3: Total pressure near the diffuser discharge (the AIP).

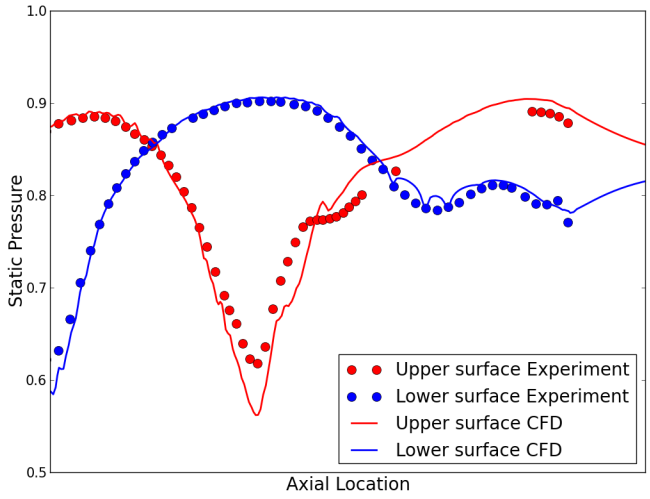

Figure 4: Comparison of CFD and experimental static pressure along the upper and lower walls.

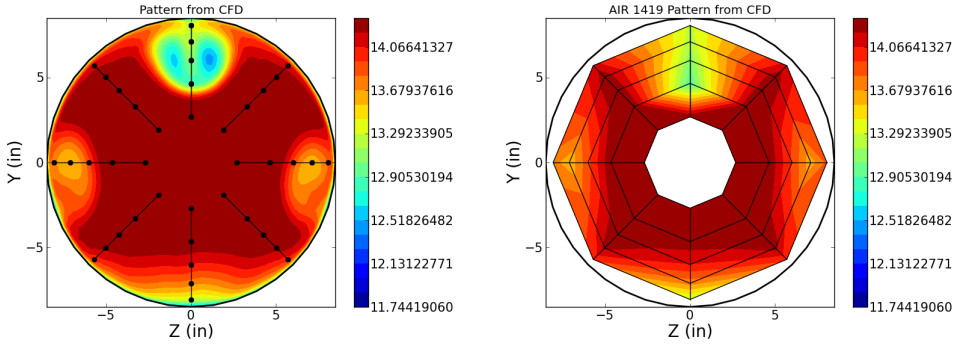

(a) Solution (b) Discrete points

Figure 5: Total pressure solution and discrete probe values for the 5×8 probe configuration.

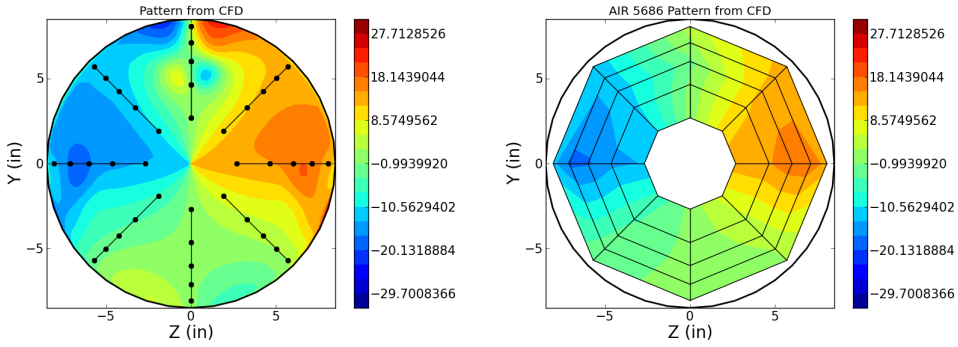

(a) Solution (b) Discrete points

Figure 6: Swirl CFD solution and discrete probe values for the 5×8 probe configuration.

	$\left(\frac{\Delta PC}{P}\right)$	θ^-	MPR	$\left(\frac{\Delta PR}{P}\right)$	SI	SD	SP
Ring 1 (hub)	0.000093	78.939763	1.890550	-0.019563	7.681347	0.000102	0.999966
Ring 2	0.043855	78.925576	1.000000	-0.007031	7.662768	-0.007931	0.992181
Ring 3	0.028268	69.361619	1.088735	0.000290	8.247871	-0.040068	0.965881
Ring 4	0.024401	56.903416	1.798594	0.009437	8.169948	0.009213	0.992874
Ring 5 (tip)	0.016503	65.838543	1.851098	0.016867	7.198353	0.067590	0.947581

Table 1: Distortion descriptors by ring for the 5×8 probe array.

Configuration	$\left(\frac{\Delta PC}{P}\right)$	θ^-	MPR	$\left(\frac{\Delta PR}{P}\right)$	SI	SD	SP
5×8	0.020735	66.835100	1.100150	0.000000	7.765591	0.004413	0.995973
10×360	0.047639	46.114129	1.266264	-0.000000	8.409388	-0.004796	1.009462

Table 2: Summary of distortion descriptors for both probe configurations.

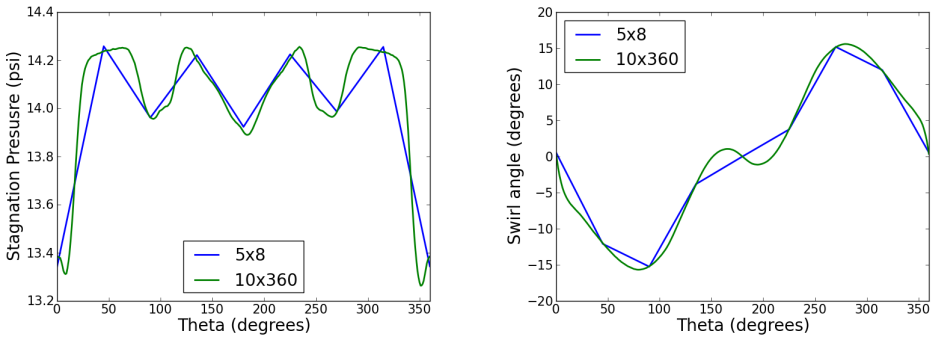

(a) Total Pressure (b) Swirl Angle

Figure 7: Face average values computed from both probe configurations.

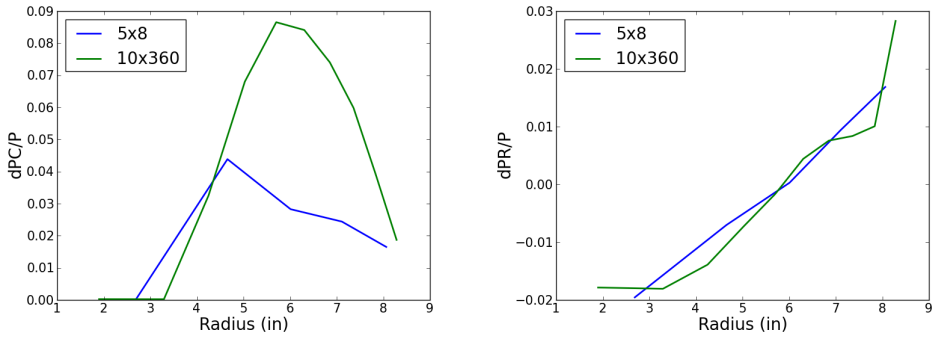

(a) $\Delta PC/P$ (b) $\Delta PR/P$

Figure 8: Circumferential and radial intensities versus probe ring radial location.

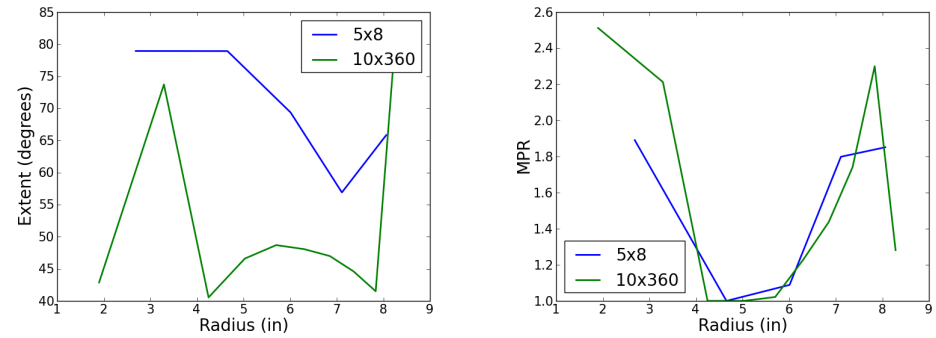

(a) Extent θ^- (b) MPR

Figure 9: Maximum circumferential extent and multiple per-rev content versus probe ring radial location.